BILINGUAL PUBLISHING GROUP

Journal of Environmental & Earth Sciences

https://journals.bilpubgroup.com/index.php/jees

ARTICLE

Rock Discontinuity Extraction from 3D Point Clouds: Application to Identifying Geological Structures in the Miocene–Pliocene Deposits, Japan

Masahiro Ohkawa [*] ***, Kota Osawa*** ***, Ryo Okino*** ***, Shigeaki Matsuo***

Mitsubishi Materials Techno Corporation, Tokyo 110-0016, Japan

ABSTRACT

Evaluating rock mass quality using three-dimensional (3D) point clouds is crucial for discontinuity extraction and is widely applied in various industrial sectors. However, the utilization of this method in geological surveys remains limited. Notable limitations of current research include the scarcity of validation using simple geometric shapes for discontinuity extraction methods, and the lack of studies that target both planar and linear discontinuity. To address these gaps, this study proposes a workflow for identifying discontinuity planes and traces in rock outcrops from photogrammetric 3D modeling, employing the Compass and Facets plugins in the open-source CloudCompare software. Prior to field application, the efficacy of the extraction methods was first evaluated using experimental datasets of a cube and an isosceles triangular prism generated under laboratory-controlled conditions. This validation demonstrated exceptional accuracy, with the dip and dip direction (DDD) of extracted structures consistently within ±2° of the actual values. Following this rigorous laboratory validation, this methodology was applied to a more complex natural rock outcrop (Miocene–Pliocene deposits in Japan), demonstrating its applicability in realistic geological settings for identifying structures. The results showed that the dip and dip direction trends of the extracted bedding planes and faults were consistent with field measurements, achieving a time reduction of approximately 40% compared to traditional methods. In conclusion, through strictly controlled initial

*CORRESPONDING AUTHOR:

Masahiro Ohkawa, Mitsubishi Materials Techno Corporation, Tokyo 110-0016, Japan; Email: maokawa@mmc.co.jp

ARTICLE INFO

Received: 22 November 2025 | Revised: 25 December 2025 | Accepted: 16 January 2026 | Published Online: 17 January 2026
DOI: https://doi.org/10.30564/jees.v8i1.12809

CITATION

Ohkawa, M., Osawa, K., Okino, R., et al., 2026. Rock Discontinuity Extraction from 3D Point Clouds: Application to Identifying Geological Structures in the Miocene–Pliocene Deposits, Japan. Journal of Environmental & Earth Sciences. 8(1): 29–46. DOI: https://doi.org/10.30564/jees.v8i1.12809

verification and subsequent successful application to a complex natural setting, this study confirmed that the proposed workflow can effectively and efficiently extract discontinuous geological structures from point clouds.
Keywords: Digital Outcrop Model; Rock Discontinuities; Geological Information; Point Cloud

1. Introduction

Rock masses are defined as blocks of rock material separated by discontinuities (e.g., joints, faults, and bedding planes)[1], and identifying these discontinuities is essential for mine planning, quarry monitoring, slope stability analysis, and tunneling[2–5]. Jaboyedoff et al.[2] used digital elevation models from airborne laser scanning to analyze structural characteristics, aiding in the understanding of progressive failure in large rock slopes. Similarly, Viero et al.[6] utilized laser scanning to detect rotational movements associated with deep-seated gravitational instabilities, highlighting the potential of three-dimensional (3D) data for monitoring dynamic geological processes in landslides. In recent years, Digital Outcrop Models (DOMs)[7], which are 3D frameworks derived from laser-scanning or photogrammetry-based surveys, have become widely used for rock discontinuity identification. Riquelme et al.[8] introduced a method for discontinuity spacing analysis directly from 3D point clouds, which showed improved accuracy and efficiency over traditional field methods. Chen et al.[9] developed an automatic method to extract discontinuity orientation from 3D point clouds of rock mass surface, streamlining characterization. Ge et al.[10] proposed an automated technique for measuring discontinuity geometric properties from 3D point clouds using a modified region growing algorithm. The Structure-from-Motion (SfM) technique, an adaptation of photogrammetry that creates 3D models from multiple overlapping images[11], is a convenient and cost-effective method for generating high-resolution DOMs[12–14]. This approach has been demonstrated to significantly reduce the time required for DOM generation and facilitate the extraction of rock discontinuities[15–17].

A review of the extant literature on rock mass discontinuities can be broadly divided into three categories: (1) discontinuity plane extraction, (2) discontinuity trace extraction, and (3) other methods, such as roughness, spacing, and block size analyses[18]. Furthermore, methods for extracting planes from point clouds can be broadly categorized as follows: (1) clustering-based methods, (2) region growing-based methods, and (3) other methods, such as random sample consensus and principal component analysis[19]. The general approach to trace extraction methods involves utilizing geometric characteristics within 3D point clouds[20,21]. Among these techniques, clustering methods have become a prominent research topic in the fields of rock mechanics and geotechnical engineering[22]. Rock discontinuity clustering has historically been based on a single parameter, primarily orientation data[9,23–26]. However, recent studies have adopted multi-parameter approaches that integrate geometric and mechanical attributes, such as trace length, aperture, roughness, and infilling materials, to enhance analytical precision[22,27,28]. Wang et al.[27] employed a combined weighting analysis method that integrates the relative weights of discontinuity orientation, trace length, aperture, roughness, and filling conditions. The study showed that the objectivity of the multi-parameter clustering results was significantly improved. Liu et al.[28] integrated manifold learning and fractal theory to analyze orientation distribution patterns and characterize multiple discontinuity features. By employing manifold learning to reveal low-dimensional structures within high-dimensional datasets, they demonstrated that orientation data could undergo dimensionality reduction. This facilitated the integration of orientation data with other features without requiring extensive algorithmic modifications. On the other hand, there is no consensus on the most suitable parameters for clustering a given set of discontinuities[22]. Therefore, current multi-parameter approaches mainly rely on the experience of experts, and complete objectivity has yet to be achieved. Rock mass discontinuity extraction is widely applied in rock engineering[4,5,18]. However, there is a paucity of literature addressing the application of rock discontinuity extraction in geological surveys[14]. Understanding the properties of rock discontinuities, such as joints, faults, and bedding planes visible on outcrop surfaces, is crucial for geological surveys. Therefore, the accurate extraction of these features provides a powerful tool for assessing geological structures in the future. Although recent studies have utilized

color variations in point clouds to detect discontinuity traces on rock surfaces [15,17], the effectiveness of this approach for extracting faults and lithological boundaries from weathered and eroded outcrops requires further investigation.

In this study, we tested the discontinuity extraction capabilities of the DOMs using the Compass and Facets plugins of CloudCompare, which is an open-source software. These plugins are designed to extract discontinuity structures from point clouds [3,15,29,30]. The Compass plugin semi-automatically extracts discontinuity traces using both general and case-specific cost functions [15]. The structural orientation of the extracted traces is estimated using least-squares plane fitting. The plugin can utilize multiple cost functions, such as color brightness, color similarity, color gradient, and curvature, making it applicable to various geological structures [15]. The Facets plugin automatically performs planar segmentation using Kd-trees or fast marching methods and calculates the dip and dip direction (DDD) of the extracted plane [29]. For instance, Chandra et al. [31] applied the Facets plugin to DOMs generated by drone-based photogrammetry to extract discontinuity planes. By measuring the DDDs of outcrop surfaces, they conducted kinematic analyses of the slope failures. Similarly, Lukačić et al. [32] utilized the Compass plugin within CloudCompare to extract rock discontinuity orientations from DOM. These extracted orientations were subsequently used as primary input data for the 3D rockfall susceptibility assessment. Sevil-Aguareles et al. [33] utilized the Compass plugin in CloudCompare to analyze the DOMs of the notches in a gypsum cave, revealing that the notch roofs consistently slope towards the modern entrance. This finding enabled them to successfully reconstruct the direction of ancient water flow. Despite these advancements, a significant limitation remains: the lack of rigorous initial validation using simple geometric shapes to confirm measurement accuracy prior to field application. Furthermore, previous studies have typically employed only one plugin, and the effectiveness of methods integrating both the Compass and Facets plugins has not been fully explored. To overcome the challenges posed by inaccurate traditional measurements, in which on-site compass-clinometer readings are susceptible to errors due to operator skill [34], we first evaluated our methodology under controlled conditions. Specifically, these discontinuity plane and trace extraction methods were first evaluated using experimental 3D datasets, a cube (3 cm side) and an isosceles triangle (1.75 cm height). Following laboratory validation, the combined discontinuity plane and trace extraction method was applied to a more complex dataset (a natural rock outcrop). This approach enabled testing the extraction of various geological structures, such as bedding planes and faults, in a realistic setting. This methodology provides a robust framework for identifying geological structures within rock outcrops.

2. Data Acquisition

2.1. Case Study 1

The verification dataset for the discontinuity structure extraction was created using 3D models of seven cubic blocks with a side length of 3 cm and one isosceles triangular prism block with a height of 1.75 cm (**Figure 1**). To verify the accuracy of the discontinuity extraction on inclined planes, the cubic and triangular prism blocks were placed on a stable surface in a laboratory environment. These models were constructed using a SfM-Multi-View Stereo (MVS) processing technology based on images acquired under strictly controlled laboratory conditions to ensure geometric fidelity.

The precise lengths and heights of each block were known, and their simple and accurate geometric shapes allowed for the direct comparison and verification of the extraction method against true and pre-defined geometries. The data obtained through this process were invaluable for quantitatively assessing the accuracy and reliability of the proposed methodology.

2.2. Case Study 2

The developed extraction methods were applied to the DOM of Miocene–Pliocene fore-arc deposits (Misaki Formation), located in the southern part of the Miura Peninsula, south-central Japan [35] (**Figures 1** and **2**). The Misaki Formation, which is up to 1300 m thick, has been extensively investigated through stratigraphic, petrological, and structural geological studies [36–40]. In this study area, the Misaki Formation is lithologically monotonous, comprising white tuffaceous mudstones, grayish-white siltstone–sandstone, and dark-greenish to black coarse-grained scoriaceous sandstone [41,42] (**Figure 1**). The tuffaceous mudstone, siltstone, and sandstone frequently show graded bedding (**Figure 1**).

The formation is highly deformed and exhibits an extremely wide variety of soft-sediment deformation structures, such as load casts, associated flame structures, dish-and-pillar structures, multilobated convolutions, chaotic deformation structures, and sedimentary veins and dykes. Additionally, the formation records evidence of multiple stages of faulting and large-scale layer-parallel shortening, such as duplex structures and imbricate thrusts [35,40,42].

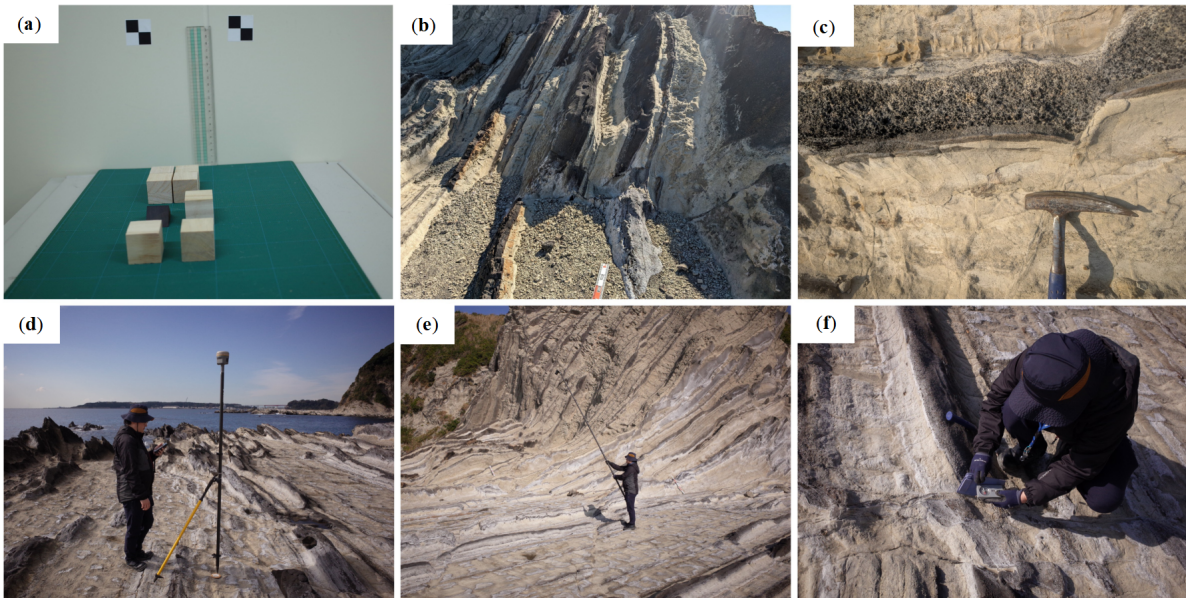

Figure 1. Field photographs from case studies 1 and 2. (**a**) Cube and isosceles triangle blocks utilized in the laboratory setting for case study 1; (**b**–**f**): Photographs from the rock outcrop for case study 2, showing: (**b**) A washboard-like relief structure with alternating layers (ridges of scoriaceous sandstone and troughs of tuffaceous mudstone and siltstone–sandstone); (**c**) Scoriaceous sandstone with normal grading and a normal fault displaying a displacement of a few centimeters; (**d**) RTK-GNSS survey; (**e**) Terrestrial photogrammetric survey; (**f**) Field geological survey.

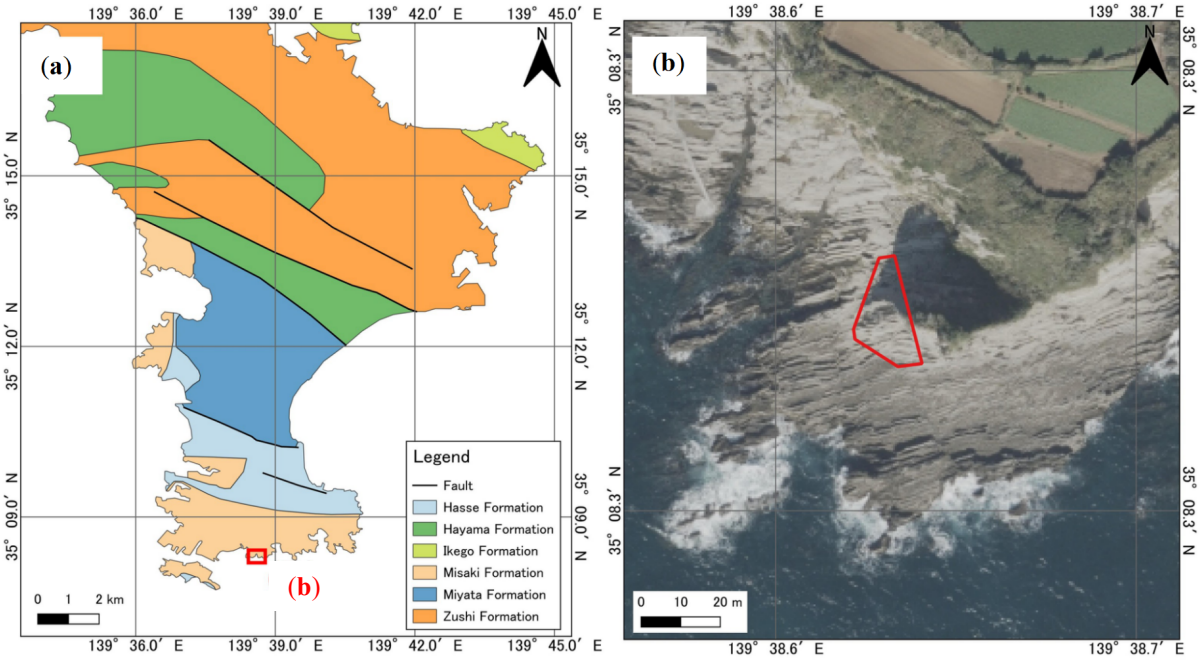

Figure 2. (**a**) Geological map of the Miura Peninsula [42]; (**b**) Location of the study area in the Miura Peninsula.

Source: The basemap image is an aerial photograph taken by the Geospatial Information Authority of Japan [43].

Despite their structural complexity, lithological variation makes it easy to distinguish between different units based on color. The area is located along the coast, and the outcrop exhibits high-quality exposure owing to the constant action of waves washing the rocks. Furthermore, the region is characterized by wave-cut benches with distinctive washboard-like relief surfaces. This topographical feature is attributed to differential erosion and weathering resistance [44]. The ridge parts of the relief are composed of scoriaceous sandstone, whereas the trough parts are composed of tuffaceous mudstone and siltstone–sandstone (**Figure 1**). Therefore, topographic information facilitates the easy tracing of structures such as bedding planes. These characteristics, that is, excellent outcrop exposure, clear lithological distinguishability, and easy structural tracing aided by topographic information, provided ideal conditions for evaluating the survey methodology and comparing it with existing approaches. Therefore, this area was selected as the study site for the present research.

3. Methods

The comprehensive workflow proposed in this study is illustrated in **Figure 3**, which is divided into two primary phases: in-situ measurement and data processing. The in-situ measurement phase involves data acquisition, including the emplacement and surveying of ground control points (GCPs) and checkpoints (CPs), image capture for photogrammetry, and manual measurement of DDDs of discontinuity data. The subsequent data processing phase consists of DOM creation using Metashape software and discontinuity extraction using the Compass and Facets plugins in CloudCompare. A detailed examination of this workflow is presented in the following sections.

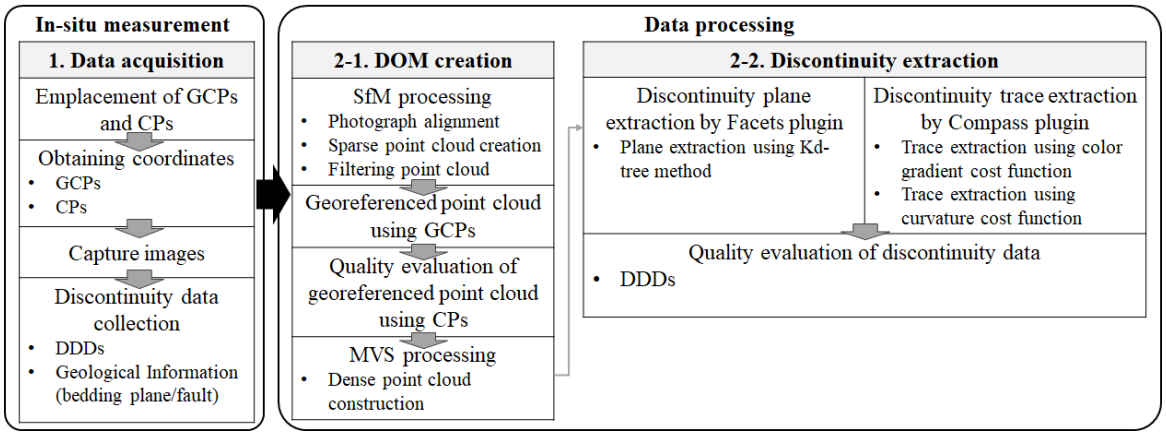

Figure 3. Proposed workflow of this study.

3.1. In-Situ Measurement

In case study 1, conducted under laboratory-controlled conditions, we first meticulously measured the length, height, and local coordinates of the cubic and isosceles triangular prism blocks. In addition, six GCPs and two CPs were emplaced, and their positions were precisely measured. These GCPs were used to transform the point cloud into a coordinate system, while CPs were used to evaluate the accuracy of the georeferenced point cloud [12,16,45]. All objects and points were photographed using a RICOH GR II digital camera with a fixed focal length of 18.3 mm (35 mm equivalent focal length of 28 mm). The images were acquired in approximately 30 min.

In case study 2 of the rock outcrop, GCPs and CPs were first placed throughout the study area. Their geographic coordinates were collected using a Real-Time Kinematic (RTK)-Global Navigation Satellite System (GNSS) survey with a Trimble R10 GNSS receiver (**Figure 1**). This georeferencing process, including the emplacement and measurement of markers, took approximately 45 min. Subsequently, a terrestrial imaging survey of the study area was performed using a RICOH GR II digital camera mounted on a monopod (**Figure 1**). Image acquisition was completed in approximately 50 min, resulting in a total data acquisition time of about 95 min for the proposed photogrammetric workflow. For comparative validation, traditional geological surveys were performed using a compass-clinometer to collect the

DDDs of bedding planes (14 structures) and faults (10 structures) in the studied outcrop (**Figure 1**). The manual process required approximately 4 h and was conducted over two separate days to verify the data and perform the remeasurements. These manual measurements were then compared with the results obtained from the DOM-based analysis. The datasets for case studies 1 and 2 comprised 159 and 218 images, respectively. The image acquisition parameters for both case studies comprised exposure times ranging from 1/125 s to 1/1600 s, f-stops between 2.8–3.5 and 2.8–6.3, and ISO values of 200 and 100–200, respectively.

3.2. Data Processing

3.2.1. DOM Creation

The DOMs were created using the SfM-MVS technique in Agisoft Metashape Professional v.2.1.3 (Agisoft LLC) (**Figures 4** and **5**). **Table 1** summarizes the specific processing conditions and parameters for both case studies 1 and 2. This software is widely used in geosciences [12,14,16,46]. The DOM creation process followed four main steps: (1) photograph alignment and sparse point cloud creation using SfM processing; (2) sparse point cloud georeferencing using measured GCPs; (3) quality evaluation of the georeferenced point cloud by comparing measured CPs coordinates with their predicted model coordinates; and (4) dense point cloud construction and DOM generation using MVS processing (**Figure 3**). All processing was performed on a 64-bit Windows 10 computer (3.0 GHz Intel Xeon Gold 6136 CPU, 128 GB RAM, and two NVIDIA Quadro P5000 GPUs) configured for optimal performance. The positional accuracy of the GCPs and CPs was specifically determined from these calculated errors, and root mean square errors (RMSEs) were calculated for the east (X), north (Y), and vertical (Z) coordinates, as well as for the total (XYZ) RMSE (**Table 2**).

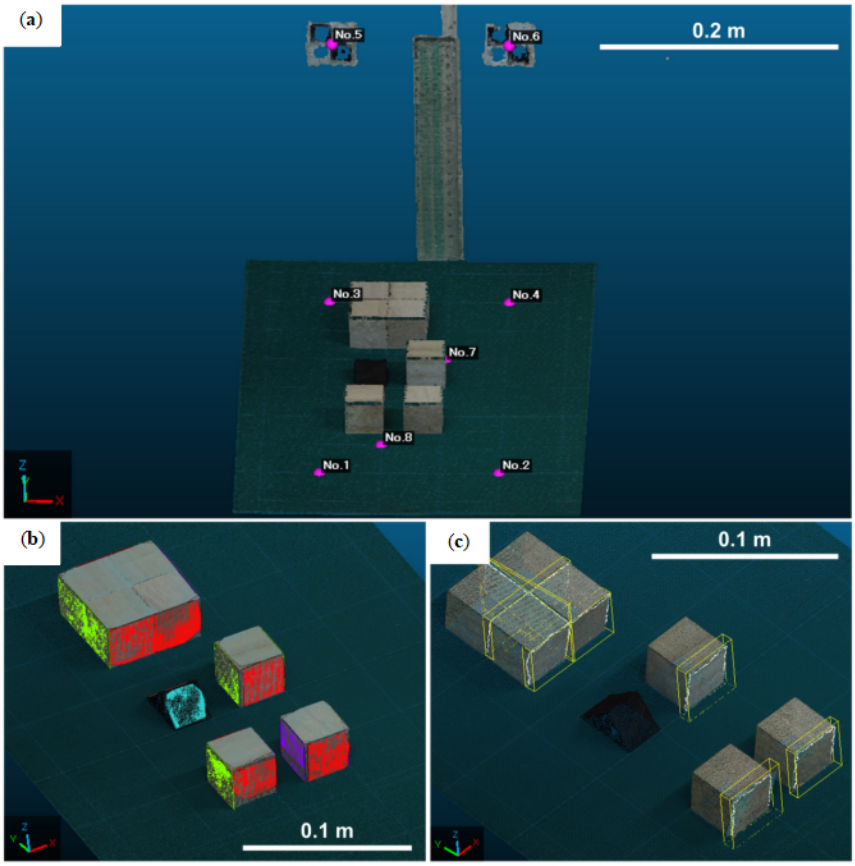

Figure 4. DOM creation and discontinuity extraction from the DOM for case study 1: (**a**) DOM generated using Metashape software. The pink circles indicate the locations of GCPs and CPs. To verify the accuracy of the extraction for inclined planes, the coordinates of the DOM were rotated so that the ground plane had a 10-degree slope; (**b**) Selected planes from the DOM extracted using the Facets plugin. The extraction surfaces are shown in red, light blue, purple, lime green, and gray; (**c**) Selected traces from the DOM extracted using the Compass plugin. The white lines and yellow areas represent the extracted trace points and their distribution ranges, respectively.

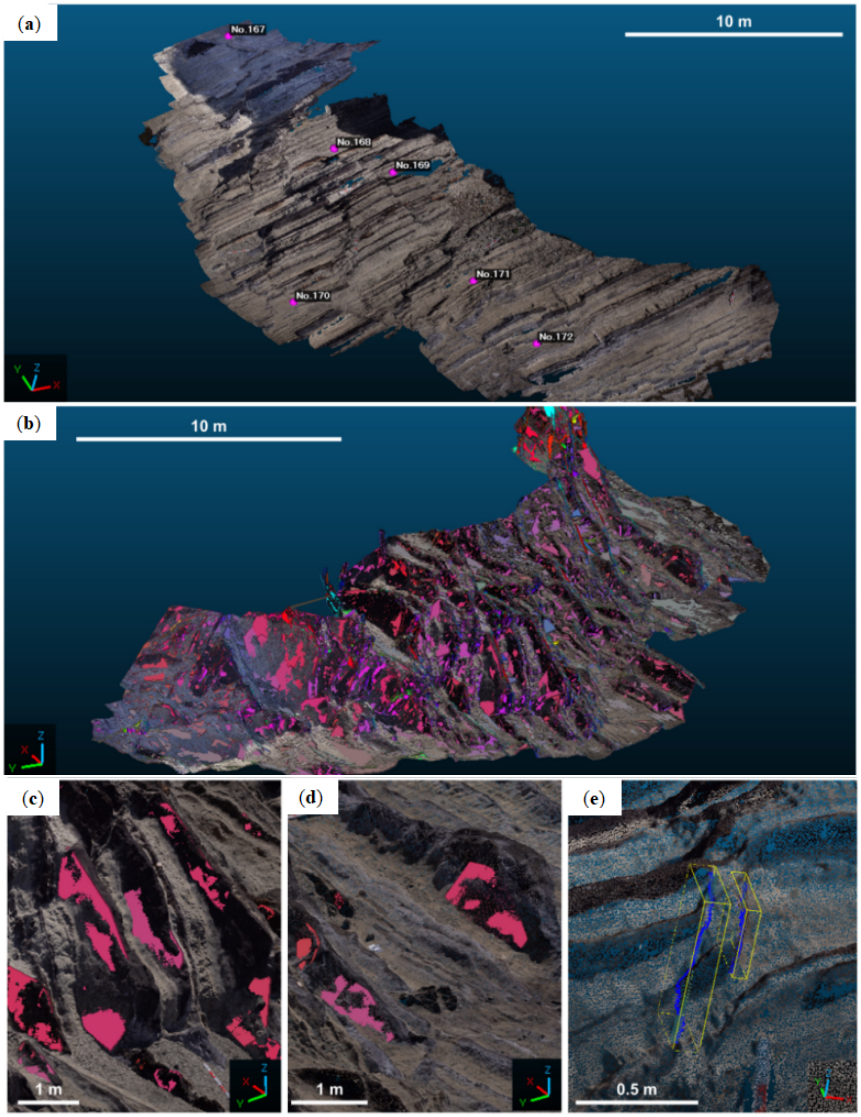

Figure 5. DOM creation and discontinuity extraction from the DOM for case study 2. (**a**) DOM generated using Metashape software. The pink circles indicate the locations of GCPs and CPs; (**b**) Discontinuity plane extraction results from the DOM using the Facets plugin; (**c**, **d**) Selected bedding planes (red areas) from the extraction results; (**e**) Selected faults from the DOM extracted using the Compass plugin. The blue lines and yellow areas represent the extracted trace points and their distribution ranges, respectively.

Table 1. Data processing parameters for DOMs creation using Metashape software and for discontinuity extraction using Facets and Compass plugins in CloudCompare software.

Parameters		Case Study 1	Case Study 2
(1) DOMs construction using Metashape software			
Number of images		159	218
Align Photos	Accuracy	Middle	Middle
	Generic preselection	Check	Check
	Reference preselection	Source	Source
	Key points limit	40,000	40,000
	Tie points limit	4000	4,000
Camera calibration		Checked all (f, b1, b2, cx, cy, k1–k4, p1, and p2)	Checked all (f, b1, b2, cx, cy, k1–k4, p1, and p2)
Build dense cloud	Quality	Middle	Low
	Depth filtering	Mild	Mild

Table 1. *Cont.*

Parameters		Case Study 1	Case Study 2
Coordinate system		Local coordinate	JGD2011 / Japan Plane Rectangular CS IX (EPSG:6677)
Metashape version		v. 2.1.3 build 18946	v. 2.1.3 build 18946
(2) Discontinuity extraction using Facets plugin			
Kd-tree cells fusion parameters	Max angle	10	10
	Max relative distance	1	1
Facets	Max distance @ 99%	0.002	0.1
	Min points per facet	10	50
	Max edge length	0.1	1
(3) Discontinuity extraction using Compass plugin			
Cost functions		Curvature RGB gradient	Curvature RGB gradient

Table 2. Accuracy of the georeferenced model evaluated using GCPs and CPs.

		X Error (m)	Y Error (m)	Z Error (m)	XYZ Error (m)
(1) Case Study 1					
GCPs	No.1	0.000	0.000	0.000	0.000
	No.2	0.000	0.000	0.000	0.000
	No.3	0.000	0.000	0.000	0.000
	No.4	0.000	−0.001	0.000	0.001
	No.5	0.000	0.000	0.000	0.001
	No.6	0.000	0.000	0.000	0.000
	Max	0.000	0.000	0.000	0.001
	Min	0.000	−0.001	0.000	0.000
	RMSE	0.000	0.000	0.000	0.000
CPs	No.7	0.000	0.000	0.000	0.001
	No.8	0.000	0.000	0.000	0.000
	Max	0.000	0.000	0.000	0.001
	Min	0.000	0.000	0.000	0.000
	RMSE	0.000	0.000	0.000	0.000
(2) Case Study 2					
GCPs	No.167	0.001	0.001	−0.007	0.007
	No.169	0.000	−0.010	0.016	0.019
	No.170	0.000	0.001	−0.003	0.003
	No.172	−0.002	0.008	−0.006	0.010
	Max	0.001	0.008	0.016	0.019
	Min	−0.002	−0.010	−0.007	0.003
	RMSE	0.001	0.007	0.010	0.012
CPs	No.168	0.007	−0.018	0.036	0.041
	No.171	0.003	−0.005	−0.012	0.013
	Max	0.007	−0.005	0.036	0.041
	Min	0.003	−0.018	−0.012	0.013
	RMSE	0.005	0.013	0.027	0.030

Note: Positive and negative values indicate that the model coordinates are greater and lower than the reference coordinates, respectively.

In SfM processing, where feature points are extracted and matched using descriptors, challenging image matching environments can introduce numerous erroneous points [47]. These errors can degrade the estimation of the surface normal and curvature [48]. Han and Han [47] reported that filtering point clouds based on confidence values effectively identifies and removes these error points in difficult areas, improving geometric quality without compromising accuracy. The Metashape software normalizes these confidence values to a range of 0–255 based on the maximum and minimum image overlap counts. To mitigate the impact of erroneous points and ensure high-quality structural extraction, the final DOMs were created by removing points from dense point clouds with low confidence (≤1).

3.2.2. Discontinuity Extraction

Discontinuity structures (both planes and traces) were identified and extracted from the DOMs using the Facets and Compass plugins in CloudCompare (**Figures 3–5**). **Table 1** summarizes the parameters used for the Facets and Compass plugins in both case studies 1 and 2.

To extract discontinuity planes, the Facets plugin was utilized to perform a fully automated segmentation of the point cloud. This process employs the Kd-tree algorithm, which recursively subdivides the point cloud into smaller cells until the points within a cell fit a best-fitting plane according to a specific root mean square threshold (referred to as the "max distance"). Subsequently, the algorithm merges adjacent cells into larger planar facets if they share a common orientation (within a specific "max angle") and are sufficiently close along their common normal[29]. To ensure the reliability of this automated process, the processing parameters, specifically the max distance threshold, were carefully determined through an iterative sensitivity analysis. We evaluated a range of threshold values for each dataset through visual inspection to determine the specific setting that most accurately preserved the typical structural shapes.

Discontinuity traces were extracted using the Compass plugin. While not a fully automated method, this tool facilitates semi-automated mapping by employing a least-cost path algorithm[15]. In this study, we carefully observed the DOMs to visually identify and distinguish specific discontinuous structures, such as faults and bedding planes. For each target feature, the start and end control points were manually defined, allowing the plugin to compute the optimal path along the structure. To mitigate errors in path generation and improve the accuracy of structural DDD estimation, any deviations in the automatically generated traces were corrected by manually adding intermediate control points, ensuring that the traces accurately followed the visible geological boundaries. The trace extraction was performed using a combination of color gradient and curvature cost functions. These specific functions were selected for their ability to effectively delineate and distinguish the boundaries of linear geological structures (faults and bedding planes) on the rock outcrop surfaces.

The validity of the extracted discontinuous structures was evaluated by comparing the results with the discontinuity data (DDDs) collected during the in-situ measurement phase. This step confirmed that the extraction methods were consistent with the field observations. Both field measurements and DOM-based analysis results were plotted and evaluated using Stereonet 11 software[49] (**Figure 6**).

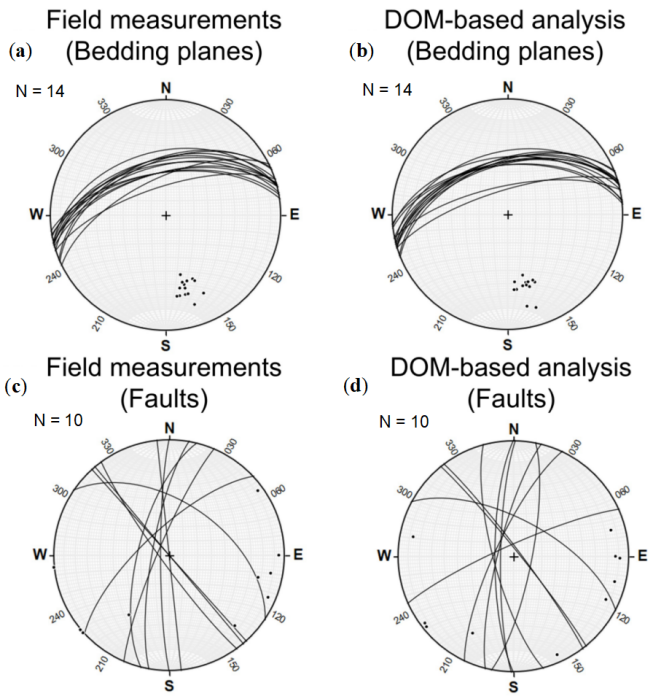

Figure 6. Stereonet plots (black points) of bedding planes from: (**a**) field measurements; (**b**) DOM-based analysis; and faults from: (**c**) field measurements; (**d**) DOM-based analysis.

4. Results

4.1. DOMs Characteristics and Accuracy

The described procedure generated DOMs for both case studies 1 and 2. Each DOM comprised 773,249 and 8,350,727 points and covered areas of approximately 1362 cm^2 and 326 m^2, respectively. By leveraging a high-performance workstation, we achieved an efficient computational process. Specifically, the DOM generation workflow for case studies 1 and 2, from photo alignment to dense cloud reconstruction, was completed in approximately 25 min per case study. **Table 2** presents a detailed comparison of the GCP and CP coordinates of the measurement results with their corresponding model coordinates. Each difference in **Table 2** represents the difference between the analytical and measured values. A positive sign indicates that the model coordinate is greater than the reference coordinate, and a negative sign indicates that the model coordinate is lower than the reference coordinate. In this process, GCPs were used for the georeferencing of the point cloud, whereas CPs were used to evaluate the accuracy of the georeferenced point cloud.

The case study 1 was conducted under strictly controlled laboratory conditions and demonstrated extremely high accuracy. The maximum XYZ errors were 0.001 m for the GCPs and CPs, and the RMSEs in XYZ were negligible at under 0.001 m for the GCPs and CPs (**Table 2**). These exceptionally low errors confirm that the DOM created from datasets obtained under laboratory-controlled conditions is highly accurate. This effectively minimizes environmental noise and human-induced biases, making it an ideal benchmark for the accuracy verification of the model. In case study 2 (rock outcrop), the accuracies of the GCPs and CPs were of the same order, with larger magnitudes than those in case study 1. Specifically, the maximum XYZ errors were 0.019 m for GCPs and 0.041 m for CPs, and the RMSEs in XYZ were 0.012 m for GCPs and 0.030 m for CPs (**Table 2**). This increase in error is attributed to the inherent precision limits of the RTK-GNSS receiver used for field measurements, as opposed to the sub-millimeter precision achieved in the laboratory using simple and accurate 3D shapes. Nevertheless, these results indicate that the generated DOM has centimeter-level positional accuracy.

4.2. Discontinuity Extraction

In case studies 1 and 2, 28 and 24 discontinuities were extracted, respectively, using the Compass and Facets plugins in CloudCompare. The extraction process identified two types of features: discontinuity planes and traces. The semi-automated extraction phase was highly time-efficient, processing the entire dataset for case studies 1 and 2 in approximately 25 min per case. The DDDs of the extracted structures were then compared with the measured field results (**Tables 3** and **4**). In **Tables 3** and **4**, the discrepancies in dip direction are expressed as clockwise (positive) or counterclockwise (negative) differences of the DOM-based results from the in-situ measurements. Conversely, for dip, a positive value shows that the in-situ measurement is larger than the DOM-based value, while a negative value indicates that the in-situ measurement is smaller.

Table 3. Comparison of the DDD for selected planes and traces in case study 1, contrasting direct measurements with those obtained through DOM-based analysis.

ID	Field Measurement		DOM-Based Analysis		Difference		Detection Methods
	Dip	Dip Direction	Dip	Dip Direction	Dip	Dip Direction	
(1) Planes (22 Structures)							
284	80	0	81	0	1	0	Facets
285	80	0	80	359	0	1	Facets
288	10	180	10	179	0	−1	Facets
289	80	0	81	359	1	1	Facets
290	90		89	269	−1		Facets
291	80	0	80	359	0	1	Facets
292	80	0	79	358	−1	2	Facets
293	55	180	54	180	−1	0	Facets
294	80	0	79	0	−1	0	Facets
295	35	0	33	0	−2	0	Facets
297	90		89	89	−1		Facets
298	90		89	270	−1		Facets

Table 3. *Cont.*

ID	Field Measurement		DOM-Based Analysis		Difference		Detection Methods
	Dip	Dip Direction	Dip	Dip Direction	Dip	Dip Direction	
(1) Planes (22 Structures)							
299	80	0	80	0	0	0	Facets
300	10	180	10	179	0	−1	Facets
302	80	0	80	359	0	1	Facets
303	90		88	89	−2		Facets
304	10	180	9	180	−1	0	Facets
305	90		89	89	−1		Facets
306	90		89	271	−1		Facets
307	90		89	88	−1		Facets
308	90		89	270	−1		Facets
309	10	180	10	180	0	0	Facets
	Max				1	2	
	Min				−2	−1	
	RMSE				1	1	
(2) Traces (6 Structures)							
1	90		90	270	0		Compass (RGB gradient)
2	80	0	80	0	0	0	Compass (RGB gradient)
3	80	0	79	0	−1	0	Compass (Curvature)
4	80	0	80	359	0	1	Compass (Curvature)
5	80	0	79	358	−1	2	Compass (Curvature)
6	80	0	78	1	−2	1	Compass (Curvature)
	Max				0	2	
	Min				−2	0	
	RMSE				1	1	

Note: For dip direction, positive and negative values indicate clockwise and counterclockwise differences of DOM from field measurements, respectively. For dip, positive and negative values indicate that the field measurements are larger or smaller than the DOM results, respectively.

Table 4. Comparison of the DDD for selected bedding planes and faults in case study 2, contrasting field measurements with those obtained through DOM-based analysis.

ID	Field Measurement		DOM-Based Analysis		Difference		Detection Methods
	Dip	Dip Direction	Dip	Dip Direction	Dip	Dip Direction	
(1) Bedding Planes (14 Structures)							
1	52	345	53	338	1	−7	Facets
5	54	349	55	353	1	4	Facets
10	50	337	51	345	1	8	Facets
21	60	350	54	344	−6	−6	Facets
22	50	342	51	339	1	−3	Facets
24	44	346	49	354	5	8	Compass (RGB gradient)
26	60	346	45	346	−15	0	Compass (RGB gradient)
27	55	345	53	345	−2	0	Facets
32	64	334	73	343	9	9	Compass (RGB gradient)
33	70	342	70	348	0	6	Compass (RGB gradient)
35	60	344	55	355	−5	11	Facets
37	52	336	55	343	3	7	Facets
44	50	346	53	348	3	2	Facets
46	60	352	51	343	−9	−9	Facets
	Max				9	−9	
	Min				−15	−9	
	RMSE				6	7	

Table 4. *Cont.*

ID	Field Measurement		DOM-Based Analysis		Difference		Detection Methods
	Dip	Dip Direction	Dip	Dip Direction	Dip	Dip Direction	
(2) Faults (10 Structures)							
1	82	293	77	295	−5	2	Compass (Curvature)
8	72	317	82	336	10	19	Compass (RGB gradient)
10	90	84	77	101	−13	17	Compass (Curvature)
12	90	48	86	51	−4	3	Compass (Curvature)
14	84	234	76	255	−8	21	Compass (Curvature)
15	52	34	64	28	12	−6	Compass (Curvature)
16	90	50	85	53	−5	3	Compass (Curvature)
17	84	270	77	270	−7	0	Compass (Curvature)
21	68	284	79	284	11	0	Compass (Curvature)
22	78	280	81	271	3	−9	Compass (Curvature)
	Max				12	−9	
	Min				−13	−9	
	RMSE				8	11	

Note: For dip direction, positive and negative values indicate clockwise and counterclockwise differences of DOM from field measurements, respectively. For dip, positive and negative values indicate that the field measurements are larger or smaller than the DOM results, respectively.

In case study 1, a comparison of the selected planes and traces revealed a DDD difference of less than ±2° between the measured values and the DOM-based results (**Table 3**). The RMSEs for the selected planes and traces were 1°, indicating no significant difference between the methods (**Table 3**). Although the Compass plugin uses semi-automated, user-guided mapping, which is less objective than fully automated methods, it is still more objective and efficient than purely manual extraction [15]. Therefore, despite the potential for some artificial bias in the trace extraction results, these results quantitatively confirm the high accuracy of DOM-based extraction under laboratory-controlled conditions. In case study 2, the DOM-based analysis successfully captured the DDD trends of the discontinuity structures. The extracted bedding planes exhibited a remarkable uniformity, consistently dipping into the NNW direction with dip angles generally ranging from 50° to 70°. This structural consistency indicates a homoclinal structure, suggesting that no significant folding or ductile deformation is present within the rock outcrop of the study area. The extracted faults were predominantly high-angle (dip angle > 70°) and generally dipped into the WNW and NE directions (**Table 4** and **Figure 6**). Overall, the stereonet plotting of the DDD results obtained from the field measurements and DOM-based analysis showed a high degree of consistency. The high concentration of poles in both datasets indicates excellent consistency between the DOM-based results and the in-situ measurements, which reveals the reliability of the extraction method.

This study demonstrates the effectiveness of the Facets and Compass plugins of CloudCompare for extracting geological planes and traces, thereby supporting their potential for the efficient mapping of entire rock outcrops. However, the differences observed in case study 2 were larger than those in the laboratory tests. The maximum absolute DDD difference between the selected planes and traces exceeded ±10° at certain sites (**Table 4**). In the selected planes, the RMSEs of the DDDs were 6° and 7°, respectively. In the selected traces, the RMSEs of the DDDs were 8° and 11°, respectively (**Table 4**).

5. Discussion

In case study 1, the comparison results of the DDDs from 22 discontinuity planes and 6 discontinuity traces revealed consistently very low differences and RMSEs (**Table 3**). This high accuracy is attributed to the creation of the

3D model from simple, geometrically precise shapes, coupled with excellent positional accuracy (**Table 2**). In this study, it was found to be essential to use datasets acquired under controlled laboratory conditions with objects of simple and accurate shapes to accurately verify the extraction of discontinuous structures. This approach introduces minimal bias that affects the quality of the point cloud, allowing for a precise evaluation of the extraction accuracy. Slight differences in the DDD values were observed between the measured and analyzed results. These discrepancies may stem from the processing parameters used for DOM creation. To manage the processing time and prevent memory overflow, the generation of the dense point cloud for case study 1 was performed at Medium Quality, downscaling images by a factor of 4. As the quality of the DOM is influenced by the image pixel resolution [12,50], resulting in smoother edges, this may have affected the quality of the discontinuity extraction. Nevertheless, these validated results provide a solid basis for extracting geological structures using DOMs in complex natural rock outcrops.

The difference in DDD between the measurement and analysis results was notably higher in case study 2 than in case study 1 (**Tables 3** and **4**). This is likely due to the complex geometry of the rock outcrops in case study 2 and the fact that the DOM was created from images acquired under outdoor conditions. As mentioned above, positional errors on the order of centimeters are inherent to the DOM generated in this environment due to the accuracy limits of the RTK-GNSS receiver. Under such conditions, the DOM quality is affected not only by the pixel resolution [12] but also by noisy pixels caused by shadows and saturation [51]. Additionally, similar to the procedure in case study 1, to manage processing time and avoid memory overflow, the dense point cloud generation for case study 2 was executed at a Low Quality, effectively downscaling the images by a factor of 8. This reduction in resolution likely compromised the repeatability of the DOM, which may have subsequently affected the accuracy of discontinuity extraction. Furthermore, several researchers have reported that the presence of non-rock objects, such as vegetation, creates noise that prevents accurate 3D model generation [31,52]. Bemis et al. [52] reported that model accuracy is often reduced by surface reflections, flat surfaces with little texture variation, and deep shadows. They also noted that detrimental lighting changes can result from self-shadowing, shadows cast by the photographer, shifts in the sun's position, or filtering by clouds. Riquelme et al. [53] reported that SfM-based DOM was highly accurate when the target surface was perpendicular to the camera axis. However, the accuracy tended to decrease at oblique angles and near the edges. Furthermore, they noted discrepancies in complex surface topographies when comparing SfM-based DOM with those obtained from terrestrial laser scanning. In case study 2, parts of the rock surface were covered by weathering products and boulders. Furthermore, the complex morphology and irregular geometry of the outcrop surface, combined with the smooth slope profile resulting from weathering and erosion, disrupted the continuity of the surface geometry, thereby complicating the segmentation process. Previous studies have indicated that some plane and trace extraction methods lack sufficient robustness when applied to rock mass data that exhibits weathering features [17,19]. Although vegetation was barely recognized on the rock outcrop in case study 2, the surrounding topographic relief obstructed sunlight, resulting in cast shadows in certain areas. Given these factors, the results in case study 2 were likely influenced by a combination of photographic and environmental conditions, the inherent precision limits of the RTK-GNSS receiver, as well as potential errors from operator skill during the comparative compass-clinometer measurements [34].

Despite these challenges, the proposed workflow has significant advantages over traditional methods, such as reducing operator errors and enhancing survey efficiency. Traditional manual measurements using a compass-clinometer are inherently subjective and susceptible to human error. Previous studies have indicated that manual compass-clinometer measurements typically have a mean error ranging from 1° to 8°, depending on the engineer's expertise and judgment [12,54,55]. In addition, these measurements are affected by systematic errors caused by magnetic interference from ferrous objects [54]. Wong et al. [56] indicated that the manual measurements may lead to problems associated with selective sampling and human bias, particularly among inexperienced practitioners. Our validation using the laboratory dataset (case study 1) demonstrated that the results from the DOM-based method were closely aligned with manual measurements. The proposed workflow relies on automated and semi-automated extraction, which enhances objectivity and

reduces human-induced biases that are typical of traditional compass-clinometer measurements. Furthermore, traditional methods require manual adjustments for magnetic declination, which is susceptible to arithmetic errors. In contrast, the proposed method automates the calculation of the DDD, effectively eliminating the risk of errors in manual calculations. The results of case study 2 also demonstrated that the DOM-based results were in strong agreement with the field measurements. While the discrepancies were larger than those observed in laboratory tests, they reflect the challenging image acquisition conditions, the precision limits of the RTK-GNSS receiver, and the inherent complexity of the natural environment. These results emphasize the critical importance of using simple, accurately defined 3D models to initially verify discontinuity extraction techniques. This step ensures that any errors observed in the field can be correctly attributed to environmental and acquisition factors rather than issues with the extraction technique.

In terms of work efficiency, the proposed workflow demonstrated a significant reduction in the field survey duration. In case study 2, the traditional geological survey required approximately 4 h of working time. This process required visits on two separate days to verify the data and perform remeasurements. In contrast, the proposed workflow was completed in a total of 145 min: approximately 50 min for image acquisition, 45 min for GCP and CP emplacement and surveying, 25 min for DOM creation, and 25 min for discontinuity extraction (**Table 5**). This represents a time reduction of approximately 40% compared to the traditional method. In particular, the DOM generation and discontinuous extraction phases were rapid. This efficiency allows geologists to dedicate more time to interpretation rather than data collection. Furthermore, the proposed method offers a significant advantage in terms of data verification and remeasurement because it enables discontinuous structures to be extracted from the DOM without requiring a return visit to the site.

Table 5. A comparison of the time requirements between the traditional and proposed methods in case study 2.

		Traditional Method	Proposed Method
Working Time (min)	In-site measurement	240	95
	DOM creation		25
	Discontinuity extraction		25
	Total	240	145

In conclusion, while challenges in photogrammetry-based DOM creation remain due to photographic and environmental conditions such as vegetation, shadows, complex topography, and eroded surfaces, the DDDs extracted from the DOM demonstrated a strong correlation with field measurements. This demonstrates that DOMs can effectively identify discontinuous geological structures, suggesting them to be valuable tools for quantitative analysis. Furthermore, this approach has significant advantages, such as reducing potential human bias, improving survey efficiency, and overcoming the limitations associated with surveys in inaccessible areas.

6. Conclusions

This study addressed the significant disparity between the widespread adoption of photogrammetric 3D modeling in rock engineering and its limited application in traditional geological surveys. A critical gap in existing research remains: the lack of rigorous validation using controlled geometries prior to field application and a limited focus on studies that integrate both planar and linear structural extraction. To bridge this gap, we introduced and validated a comprehensive workflow for identifying discontinuity planes and traces using an SfM-based photogrammetric approach integrated with the Facets and Compass plugins in CloudCompare. We then implemented a two-stage validation approach to evaluate this workflow. First, we evaluated the extraction techniques using experimental datasets of a cube and an isosceles triangular prism generated under strictly controlled laboratory conditions (case study 1). The use of these precise, known geometries established an invaluable baseline for assessing the intrinsic performance of the algorithms. The results from this phase demonstrated high geometric fidelity, with extremely low RMSEs for both the position and DDD compared to the field measurements. This quantitatively confirmed that the proposed extraction workflow achieved high accuracy under ideal conditions, where environmental noise and human-induced biases were minimized. Following this laboratory validation, the methodology was applied to a complex natu-

ral rock outcrop of the Misaki Formation (case study 2) to demonstrate its practical applicability in a realistic geological setting. Despite the challenges posed by irregular surface topography, weathering, and erosion, the DOM-based analysis successfully identified geological structures, including bedding planes and high-angle faults. These results showed a strong correlation with in-situ measurements, confirming the reliability of the method for determining structural trends.

This study also emphasized the significant improvements in the survey efficiency and data objectivity. The proposed workflow reduced the time required for the survey by approximately 40% compared to traditional methods. Specifically, the entire process, from image acquisition to discontinuity extraction, was completed in 145 min, whereas traditional surveys required approximately 4 h. Notably, DOM creation and extraction phases were rapid. Furthermore, by automating or semi-automating the extraction processes, the workflow effectively mitigates the human-induced biases associated with traditional compass-clinometer measurements. However, certain limitations remain. While the laboratory results showed negligible errors, the field applications revealed that the precision of 3D models was influenced by the measurement and environmental conditions. Therefore, we emphasize the critical importance of using simple, accurately defined 3D models for the initial verification of discontinuity extraction techniques. This step ensures that any errors observed in the field can be correctly attributed to environmental and acquisition factors rather than issues with the extraction technique. In conclusion, the proposed workflow offers a robust, efficient, and highly accurate framework for identifying geological structures from point clouds.

Author Contributions

Conceptualization, M.O. and K.O.; methodology, M.O.; validation, M.O.; formal analysis, M.O.; investigation, M.O., K.O., R.O. and S.M.; data curation, M.O.; writing—original draft preparation, M.O.; writing—review and editing, M.O. and K.O.; visualization, M.O.; supervision, M.O. and K.O.; project administration, K.O. All authors have read and agreed to the published version of the manuscript.

Funding

This work received no external funding.

Institutional Review Board Statement

Not applicable.

Informed Consent Statement

Not applicable.

Data Availability Statement

The data that support the findings of this study are available from the corresponding author upon reasonable request.

Acknowledgments

The previous version of the manuscript was improved by the helpful comments of Dr. Hasegawa and three anonymous reviewers. Furthermore, this paper has benefited from the valuable feedback provided by the editor and the anonymous reviewer.

Conflicts of Interest

The authors declare that they have no competing financial interests or personal relationships that could influence the work reported in this study.

References

[1] Bieniawski, Z.T., 1989. Engineering Rock Mass Classifications: A Complete Manual for Engineers and Geologists in Mining, Civil, and Petroleum Engineering. John Wiley & Sons: New York, NY, USA. pp. 1–251.

[2] Jaboyedoff, M., Couture, R., Locat, P., 2009. Structural analysis of Turtle Mountain (Alberta) using digital elevation model: Toward a progressive failure. Geomorphology. 103(1), 5–16.

[3] Nagendran, S.K., Ismail, M.A.M., Wen, Y.T., 2019. Photogrammetry approach on geological plane extraction using CloudCompare FACET plugin and scanline survey. Bulletin of the Geological Society of Malaysia. 68, 151–158.

[4] Kong, D., Wu, F., Saroglou, C., 2020. Automatic identification and characterization of discontinuities in rock masses from 3D point clouds. Engineering Geology. 265, 105442. DOI: https://doi.org/10.1016/j.enggeo.2019.105442

[5] Singh, S.K., Banerjee, B.P., Lato, M.J., et al., 2022. Automated rock mass discontinuity set characterisation using amplitude and phase decomposition of point cloud data. International Journal of Rock Mechanics and Mining Sciences. 152, 105072.

[6] Viero, A., Teza, G., Massironi, M., et al., 2010. Laser scanning-based recognition of rotational movements on a deep seated gravitational instability: The Cinque Torri case (North-Eastern Italian Alps). Geomorphology. 122, 191–204.

[7] Bellian, J.A., Kerans, C., Jennette, D.C., 2005. Digital outcrop models: Applications of terrestrial scanning lidar technology in stratigraphic modeling. Journal of Sedimentary Research. 75(2), 166–176. DOI: https://doi.org/10.2110/jsr.2005.013

[8] Riquelme, A.J., Abellán, A., Tomás, R., 2015. Discontinuity spacing analysis in rock masses using 3D point clouds. Engineering Geology. 195, 185–195.

[9] Chen, J., Zhu, H., Li, X., 2016. Automatic extraction of discontinuity orientation from rock mass surface 3D point cloud. Computers & Geosciences. 95, 18–31.

[10] Ge, Y., Tang, H., Xia, D., et al., 2018. Automated measurements of discontinuity geometric properties from a 3D-point cloud based on a modified region growing algorithm. Engineering Geology. 242, 44–54.

[11] Snavely, N., Seitz, S.M., Szeliski, R., 2008. Modeling the world from internet photo collections. International Journal of Computer Vision. 80, 189–210.

[12] Cawood, A.J., Bond, C.E., Howell, J.A., et al., 2017. LiDAR, UAV or compass-clinometer? Accuracy, coverage and the effects on structural models. Journal of Structural Geology. 98, 67–82.

[13] Nesbit, P.R., Durkin, P.R., Hugenholtz, C.H., et al., 2018. 3-D stratigraphic mapping using a digital outcrop model derived from UAV images and structure-from-motion photogrammetry. Geosphere. 14, 2469–2486.

[14] Cirillo, D., Cerritelli, F., Agostini, S., et al., 2022. Integrating post-processing kinematic (PPK)–structure-from-motion (SfM) with unmanned aerial vehicle (UAV) photogrammetry and digital field mapping for structural geological analysis. ISPRS International Journal of Geo-Information. 11, 437.

[15] Thiele, S.T., Grose, L., Samsu, A., et al., 2017. Rapid, semi-automatic fracture and contact mapping for point clouds, images and geophysical data. Solid Earth. 8, 1241–1253.

[16] Menegoni, N., Giordan, D., Perotti, C., et al., 2019. Detection and geometric characterization of rock mass discontinuities using a 3D high-resolution digital outcrop model generated from RPAS imagery–Ormea rock slope, Italy. Engineering Geology. 252, 145–163.

[17] Guo, J., Zhang, Z., Mao, Y., et al., 2022. Automatic extraction of discontinuity traces from 3D rock mass point clouds considering the influence of light shadows and color change. Remote Sensing. 14, 5314.

[18] Chen, J., Fang, Q., Zhang, D., et al., 2023. A critical review of automated extraction of rock mass parameters using 3D point cloud data. Intelligent Transportation Infrastructure. 2, liad005.

[19] Battulwar, R., Zare-Naghadehi, M., Emami, E., et al., 2021. A state-of-the-art review of automated extraction of rock mass discontinuity characteristics using three-dimensional surface models. Journal of Rock Mechanics and Geotechnical Engineering. 13(4), 920–936.

[20] Bazazian, D., Casas, J.R., Ruiz-Hidalgo, J., 2015. Fast and robust edge extraction in unorganized point clouds. In Proceedings of the 2015 International Conference on Digital Image Computing: Techniques and Applications, Adelaide, Australia, 23–25 November 2015; pp. 1–8.

[21] Guo, J., Wu, L., Zhang, M., et al., 2018. Towards automatic discontinuity trace extraction from rock mass point cloud without triangulation. International Journal of Rock Mechanics and Mining Sciences. 112, 226–237.

[22] Pu, C., Zhan, J., Zhang, W., et al., 2025. Characterization and clustering of rock discontinuity sets: A review. Journal of Rock Mechanics and Geotechnical Engineering. 17(2), 1240–1262.

[23] Yi, X., Feng, W., Wang, D., et al., 2023. An efficient method for extracting and clustering rock mass discontinuities from 3D point clouds. Acta Geotechnica. 18(7), 3485–3503.

[24] Gu, Z., Xiong, X., Yang, C., et al., 2024. A method for identification rock mass discontinuities in underground drift with pre-separation of linear and planar point cloud features. Ain Shams Engineering Journal. 15(12), 103110.

[25] Liu, Y., Hua, W., Chen, Q., et al., 2024. Characterization of complex rock mass discontinuities from LiDAR point clouds. Remote Sensing. 16(17), 3291.

[26] Yi, X., Wu, W., Feng, W., et al., 2025. Rock discontinuity extraction from 3D point clouds using pointwise clustering algorithm. Journal of Rock Mechanics and Geotechnical Engineering. 17(7), 4429–4444.

[27] Wang, S., Dong, F., Zhang, Z., et al., 2023. Multi-index dominant grouping of rock mass discontinuities based on the combined weighting method: A case study for the Huayang tunnel. Tunnelling and Underground Space Technology. 139, 105211.

[28] Liu, Y., Chen, J., Tan, C., et al., 2023. A novel system for multivariate analysis of discontinuities in fractured rock masses based on manifold learning and fractal models. International Journal of Rock Mechanics and Mining Sciences. 170, 105547.

[29] Dewez, T.J., Girardeau-Montaut, D., Allanic, C., et al., 2016. Facets: A CloudCompare plugin to extract geological planes from unstructured 3D point clouds.

ISPRS International Archives of the Photogrammetry, Remote Sensing and Spatial Information Sciences. 41, 799–804.

[30] Panigrahi, B., Srivastava, D.C., Tiwari, S., et al., 2023. Application of semi-automated methods for extraction of geological surface orientations: A case study from the outer Garhwal Himalaya. Journal of Earth System Science. 132, 171.

[31] Chandra, A.P., Setianto, A., Indrawan, I.G.B., 2024. Discontinuity measurement for slope failure analysis with structure from motion method using drone on a slope in Hargowilis, Kokap District, Kulon Progo Regency, DI Yogyakarta Province. IOP Conference Series: Earth and Environmental Science. 1378(1), 012014.

[32] Lukačić, H., Katić, J., Bernat Gazibara, S., et al., 2024. Rapid 3D rockfall susceptibility assessment of the Orašac rock slope, Croatia. In Proceedings of the 6th Regional Symposium on Landslides in the Adriatic-Balkan Region, Belgrade, Serbia, 15–18 May 2024; pp. 213–218.

[33] Sevil-Aguareles, J., Pisani, L., Chiarini, V., et al., 2025. Gypsum cave notches and their palaeoenvironmental significance: A combined morphometric study using terrestrial laser scanning, traditional cave mapping, and geomorphological observations. Geomorphology. 471, 109576.

[34] Lee, S., Suh, J., Park, H.D., 2013. Smart compass-clinometer: A smartphone application for easy and rapid geological site investigation. Computers & Geosciences. 61, 32–42.

[35] Yamamoto, Y., Mukoyoshi, H., Ogawa, Y., 2005. Structural characteristics of shallowly buried accretionary prism: Rapidly uplifted Neogene accreted sediments on the Miura–Boso Peninsula, central Japan. Tectonics. 24, TC5008.

[36] Ogawa, Y., 1978. Structural characteristics and tectonisms around the microcontinent in the outer margin of the Paleozoic–Mesozoic geosyncline of Japan. Tectonophysics. 47(3–4), 295–310.

[37] Ogawa, Y., 1982. Tectonics of some forearc fold belts in and around the arc–arc crossing area in central Japan. Geological Society, London, Special Publications. 10(1), 49–61.

[38] Kodama, K., Oka, S., Mitsunashi, T., 1980. Geology of the Misaki District, Quadrangle Series, Scale 1:50,000. Geological Survey of Japan (AIST): Tsukuba, Japan. Available from: https://www.gsj.jp/Map/EN/docs/5man_doc/08/08_093.htm

[39] Pickering, K.T., Agar, S.M., Prior, D.J., 1990. Vein structure and the role of pore fluids in early wet-sediment deformation, Late Miocene volcaniclastic rocks, Miura Group, SE Japan. Geological Society, London, Special Publications. 54(1), 417–430.

[40] Yamamoto, Y., Ohta, Y., Ogawa, Y., 2000. Implication for the two-stage layer-parallel faults in the context of the Izu forearc collision zone: Examples from the Miura accretionary prism, central Japan. Tectonophysics. 325, 133–144.

[41] Stow, D.A., Taira, A., Ogawa, Y., et al., 1998. Volcaniclastic sediments, process interaction and depositional setting of the Mio–Pliocene Miura Group, SE Japan. Sedimentary Geology. 115, 351–381.

[42] Mazumder, R., van Loon, A.T., Malviya, V.P., et al., 2016. Soft-sediment deformation structures in the Mio–Pliocene Misaki Formation within alternating deep-sea clays and volcanic ashes (Miura Peninsula, Japan). Sedimentary Geology. 344, 323–335.

[43] Geospatial Information Authority of Japan. Map and aerial photograph service. Available from: https://service.gsi.go.jp/map-photos/app/map (cited 15 July 2021). (in Japanese)

[44] Suzuki, T., Takahashi, K.I., Sunamura, T., et al., 1970. Rock mechanics on the formation of washboard-like relief on wave-cut benches at Arasaki, Miura Peninsula, Japan. Geographical Review of Japan. 43(4), 211–222. (in Japanese)

[45] Gonçalves, G., Gonçalves, D., Gómez-Gutiérrez, Á., et al., 2021. 3D reconstruction of coastal cliffs from fixed-wing and multi-rotor UAS: Impact of SfM–MVS processing parameters, image redundancy and acquisition geometry. Remote Sensing. 13(6), 1222.

[46] Lin, J., Wang, R., Li, L., et al., 2019. A workflow of SfM-based digital outcrop reconstruction using Agisoft PhotoScan. In Proceedings of the 2019 IEEE 4th International Conference on Image, Vision and Computing (ICIVC), Xiamen, China, 5–7 July 2019; pp. 711–715.

[47] Han, S., Han, D., 2024. Enhancing direct georeferencing using real-time kinematic UAVs and structure-from-motion-based photogrammetry for large-scale infrastructure. Drones. 8(12), 736.

[48] Daghigh, H., Tannant, D.D., Daghigh, V., et al., 2022. A critical review of discontinuity plane extraction from 3D point cloud data of rock mass surfaces. Computers & Geosciences. 169, 105241.

[49] Cardozo, N., Allmendinger, R.W., 2013. Spherical projections with OSXStereonet. Computers & Geosciences. 51, 193–205.

[50] Monsalve, A., Yager, E.M., Tonina, D., 2023. Evaluating Apple iPhone LiDAR measurements of topography and roughness elements in coarse bedded streams. Journal of Ecohydraulics. 10(2), 181–191.

[51] Ivelja, T., Bechor, B., Hasan, O., et al., 2020. Improving vertical accuracy of UAV digital surface models by introducing terrestrial laser scans on a point-cloud level. International Archives of the Photogrammetry, Remote Sensing and Spatial Information Sciences. XLIII-B1-2020, 457–463.

[52] Bemis, S.P., Micklethwaite, S., Turner, D., et al., 2014. Ground-based and UAV-based photogrammetry: A multi-scale, high-resolution mapping tool for structural geology and paleoseismology. Journal of Structural Geology. 69, 163–178.

[53] Riquelme, A., Cano, M., Tomás, R., et al., 2017. Identification of rock slope discontinuity sets from laser scanner and photogrammetric point clouds: A comparative analysis. Procedia Engineering. 191, 838–845.

[54] Novakova, L., Pavlis, T.L., 2017. Assessment of the precision of smart phones and tablets for measurement of planar orientations: A case study. Journal of Structural Geology. 97, 93–103.

[55] Benrabah, A., Senent Domínguez, S., Carrera-Ramírez, F., et al., 2023. Structural and geomechanical analysis of natural caves and rock shelters: Comparison between manual and remote sensing discontinuity data gathering. Remote Sensing. 16(1), 72.

[56] Wong, D., Chan, K., Millis, S., 2019. Digital mapping of discontinuities. In Proceedings of the 39th HKIE Geotechnical Division Annual Seminar, Hong Kong, China, 11 April 2019; p. 13.